ADVANCED MATERIALS
www.advmat.de

Suppressing Charged Cation Antisites via Se Vapor Annealing Enables p-Type Dopability in $AgBiSe_2$–SnSe Thermoelectrics

Hanhwi Jang, Michael Y. Toriyama, Stanley Abbey, Brakowaa Frimpong, James P. Male, G. Jeffrey Snyder, Yeon Sik Jung,* and Min-Wook Oh**

Cation disordering is commonly found in multinary cubic compounds, but its effect on electronic properties has been neglected because of difficulties in determining the ordered structure and defect energetics. An absence of rational understanding of the point defects present has led to poor reproducibility and uncontrolled conduction type. $AgBiSe_2$ is a representative compound that suffers from poor reproducibility of thermoelectric properties, while the origins of its intrinsic n-type conductivity remain speculative. Here, it is demonstrated that cation disordering is facilitated by Bi_{Ag} charged antisite defects in cubic $AgBiSe_2$ which also act as a principal donor defect that greatly controls the electronic properties. Using density functional theory calculations and in situ Raman spectroscopy, how saturation annealing with selenium vapor can stabilize p-type conductivity in cubic $AgBiSe_2$ alloyed with SnSe at high temperatures is elucidated. With stable and controlled hole concentration, a peak is observed in the weighted mobility and the density-of-states effective mass in $AgBiSnSe_3$, implying an increased valley degeneracy in this system. These findings corroborate the importance of considering the defect energetics for exploring the dopability of ternary thermoelectric chalcogenides and engineering electronic bands by controlling self-doping.

1. Introduction

Thermoelectric (TE) materials enable a direct conversion of heat into electricity without mechanical moving parts, which ensures compact and reliable power generation under silent operation.[1] However, the considerably low conversion efficiency of the TE process has limited the application of TE materials.[2] Ideally, the TE efficiency can be improved by increasing the dimensionless figure-of-merit (zT) of a TE material, which is given by $zT = S^2\sigma T/\kappa$, where S, σ, T, and κ are the Seebeck coefficient, electrical conductivity, absolute temperature, and thermal conductivity, respectively.[3] Nevertheless, the competing interplay between electrical and thermal properties has stagnated the rise of zT for decades.[4]

Ternary ABX_2-type (A = group I, B = group V, X = group VI elements) compounds have gained considerable attention as promising candidates for TE applications.[5] Lone-pair electrons of B-site cations contribute to strong phonon–phonon interactions and lower the lattice thermal conductivity.[6] Therefore, several ABX_2 compounds show temperature-independent thermal conductivities unlike those of conventional TE materials.[7] This intriguing property provides a venue for modulating electronic properties with more degrees of freedom because ABX_2 compounds are relatively free from the complicated trade-off relationship between electrical and thermal properties.

However, utilizing ABX_2 compounds has been limited by serious problems: an absence of rational design rules, complex phase stability, and poor reproducibility.[8,9] For example, an undoped hexagonal $AgBiSe_2$ shows a wide range of Seebeck coefficients from –450 to 250 μV K^{-1} depending on the synthesis condition (**Figure 1**a,b). In addition, the B-site cation determines the sign of the Seebeck coefficient, where most Sb-based ABX_2 compounds are intrinsically p-type and Bi-based

H. Jang, Y. S. Jung
Department of Materials Science and Engineering
Korea Advanced Institute of Science and Technology (KAIST)
Daejeon 34141, Republic of Korea
E-mail: ysjung@kaist.ac.kr

The ORCID identification number(s) for the author(s) of this article can be found under https://doi.org/10.1002/adma.202204132.

DOI: 10.1002/adma.202204132

M. Y. Toriyama, J. P. Male, G. J. Snyder
Department of Materials Science and Engineering
Northwestern University
Evanston, IL 60208, USA
E-mail: jeff.snyder@northwestern.edu

S. Abbey, B. Frimpong, M.-W. Oh
Department of Materials Science and Engineering
Hanbat National University
Yuseong-gu, Daejeon 34158, Republic of Korea
E-mail: mwoh@hanbat.ac.kr

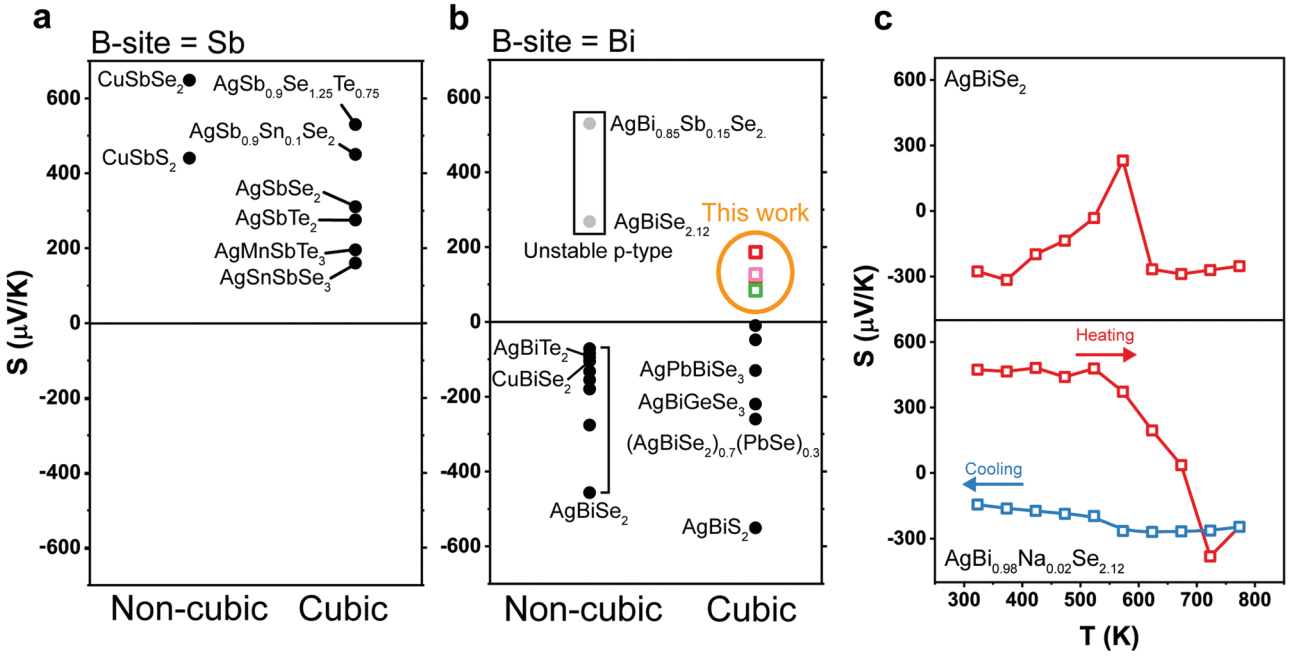

Figure 1. While the B-site cation in ABX_2 often determines whether a synthesized material is n-type or p-type, that can change with annealing. a,b) Reported Seebeck coefficient of ABX_2-type chalcogenides where the B-site cation is Sb (a) and Bi (b). Seebeck coefficients of several $AgBiSe_2$–SnSe alloys are shown in an orange circle, where p-type conductivity was stabilized by Se vapor annealing. c) Temperature-dependent Seebeck coefficient of pristine $AgBiSe_2$ and $AgBi_{0.98}Na_{0.02}Se_{2.12}$ showing an unstable p-type conductivity.

ABX_2 compounds are mostly n-type. However, bipolar doping (i.e., the ability to dope a material both n- and p-type) of ABX_2 compounds has been extremely difficult, presumably because of unknown point defects that depend on the B-site cation. Bipolar dopability is not only important for comparing carrier transport properties of electrons and holes but also for developing a practical TE module with n- and p-type legs. Therefore, it is imperative to understand the underlying defect energetics in ABX_2 compounds.

In this work, we chose $AgBiSe_2$ as a model system that suffers from poor reproducibility and uncontrolled conduction type. To exclude abrupt volume changes from its polymorphic transition, we stabilized cubic $AgBiSe_2$ by SnSe alloying to increase the configurational entropy and to reduce the phase transition temperature. We found experimental evidence of nanoscale inhomogeneities and cation ordering at room temperature from microscopic characterizations. However, we observed a disordering of cations at high temperatures via in situ Raman spectroscopy, resulting in poor p-type dopability. First-principles calculations revealed that Bi_{Ag} antisite defects were responsible for the n-type conductivity of $AgBiSe_2$, from which we speculate that cation disordering is responsible for the difficulty in stabilizing p-type $AgBiSe_2$-based alloys. Then, we employed a saturation annealing technique to suppress the formation of Bi_{Ag} in $AgBiSe_2$ alloys and to control the doping concentration to systematically analyze TE properties. As a result, we achieved a stable cubic p-type $AgBiSe_2$-based material showing a high Seebeck coefficient ranging from 80 to 190 μV K^{-1} for the first time. Our findings not only shed light on developing novel p-type ABX_2 compounds but also emphasize the importance of phase boundary effects in chalcogenide-based thermoelectrics.

2. Results

2.1. Stabilizing Cubic Phase of $AgBiSe_2$ via Entropy Engineering

As depicted in **Figure 2**a, $AgBiSe_2$ crystallizes in a hexagonal structure (space group: *P*-3*m*1, crystal system: trigonal) at room temperature.[10] In this structure, Bi atoms occupy two different crystallographic sites: one directly bonding with Se and the other intercalated between two Ag–Bi–Se layers.[11] However, these Bi atoms experience a considerable change of bonding environment upon heating due to temperature-dependent phase transitions, resulting in an abrupt change in the formation energy of point defects and overall electrical properties. For example, we synthesized p-type $AgBiSe_2$ with excess Se doped with Na; however, $AgBiSe_2$ lost the p-type character starting from 573 K and irreversibly changed to an n-type semiconductor (Figure 1c). Differential scanning calorimetry (DSC) results in Figure 2c show that pure $AgBiSe_2$ experiences a hexagonal-to-rhombohedral transition at 500 K and rhombohedral-to-cubic transition at 570 K. Based on DSC and electrical properties, we speculate that a large volume change of $AgBiSe_2$ at 573 K generates a number of donor defects, pinning the Fermi level inside the conduction bands. Therefore, suppressing the polymorphic transition in $AgBiSe_2$ is required for stable p-type conduction.

It is known that alloying several elements in a single system increases configurational entropy and stabilizes high-symmetry crystal structures at low temperatures.[12] In fact, several new cubic materials have been discovered by alloying $AgBiSe_2$ with GeSe,[13] SnSe,[14] and PbSe.[15,16] Given the cost-effectiveness and low toxicity of Sn, we chose SnSe as an alloying agent for stabilizing cubic $AgBiSe_2$. The powder X-ray diffraction (XRD)

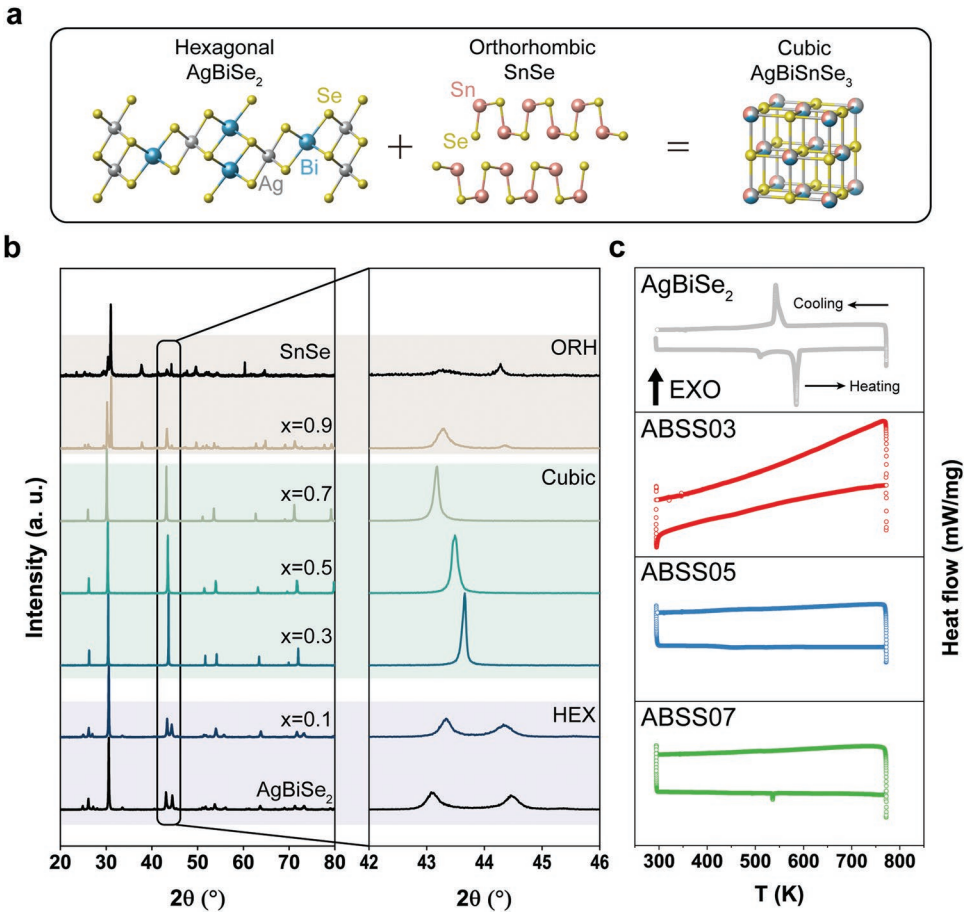

Figure 2. Regulating polymorphic behavior of $AgBiSe_2$ by alloying SnSe. a) Crystal structure of hexagonal $AgBiSe_2$, orthorhombic SnSe, and cubic $AgBiSnSe_3$. b) Powder XRD patterns of $(AgBiSe_2)_{1-x}(SnSe)_x$ alloys at 298 K. c) DSC results of pure $AgBiSe_2$ and ABSS alloys. Increasing configurational entropy decreases the enthalpy required to have a polymorphic transition, and stabilizes the cubic phase at room temperature.

patterns of $(AgBiSe_2)_{1-x}(SnSe)_x$ alloys (hereinafter, "ABSS") in Figure 2b show that the alloy adopts a cubic phase for $0.3 \leq x \leq 0.7$, while cubic and orthorhombic phases are both present for $x = 0.9$ at room temperature. Except for $x = 0.9$, secondary phases were not detected within the detection limit of the XRD technique, and solid solution behavior was observed in both the lattice parameter and the speed of sound measurements (Figures S1 and S2, Supporting Information). DSC analyses were also performed on ABSS alloys, and the endothermic peak for polymorphic transition disappeared for ABSS03 ($x = 0.3$), 05, and 07. An unidentified weak endothermic peak was observed at 537 K in ABSS07, which was ascribed to marginal atomic movements similar to $AgBiSe_2$–PbSe systems.[16] However, the detailed mechanism on this endothermic peak is not fully explained yet.

2.2. Order–Disorder Transition of Cations in ABSS05

Cubic $AgBiSe_2$ has long been considered a rock-salt compound, where cation sites are fully disordered with the same occupancy.[10,17] However, with combined spectroscopic and microscopic evidence, we reveal that cation disordering is predominant at high temperatures, while relatively suppressed at room temperature. **Figure 3**a shows an atomic-resolution scanning transmission electron microscopy (STEM) image of the matrix acquired by a high-angle annular dark-field (HAADF) detector along the [1–10] zone axis, where contrast ripples periodically appear along the [110] direction. Multislice simulation on HAADF images confirmed that brighter spots are cation sites; therefore, these contrast ripples are a signature of cation ordering (Figure S3, Supporting Information). Similar features were also observed in high-resolution transmission electron microscopy (HRTEM) image, which reveals superstructure spots in the fast Fourier transform (FFT) patterns (Figure 3b).

Cation ordering has been also observed in $AgSbTe_2$ and is known as "spontaneous nanostructures" because alternating cation configurations result in periodic nanoscale strain ripples.[18] From first-principles calculations[19] and single-crystal XRD analyses,[20] it has been suggested that two atomic configurations—the $L1_1$ (AF-II) and $D4$ (AF-IIb) structures—are most favorable due to the low formation energy among possible structures. Nevertheless, the $L1_1$ and $D4$ structures are nearly energetically degenerate, forming locally ordered nanostructures.[11,19,21] The spontaneous nanostructure of $AgSbTe_2$ consists of nanodomains with a period of 3 nm,[18] which is in agreement with the period obtained from the HAADF intensity

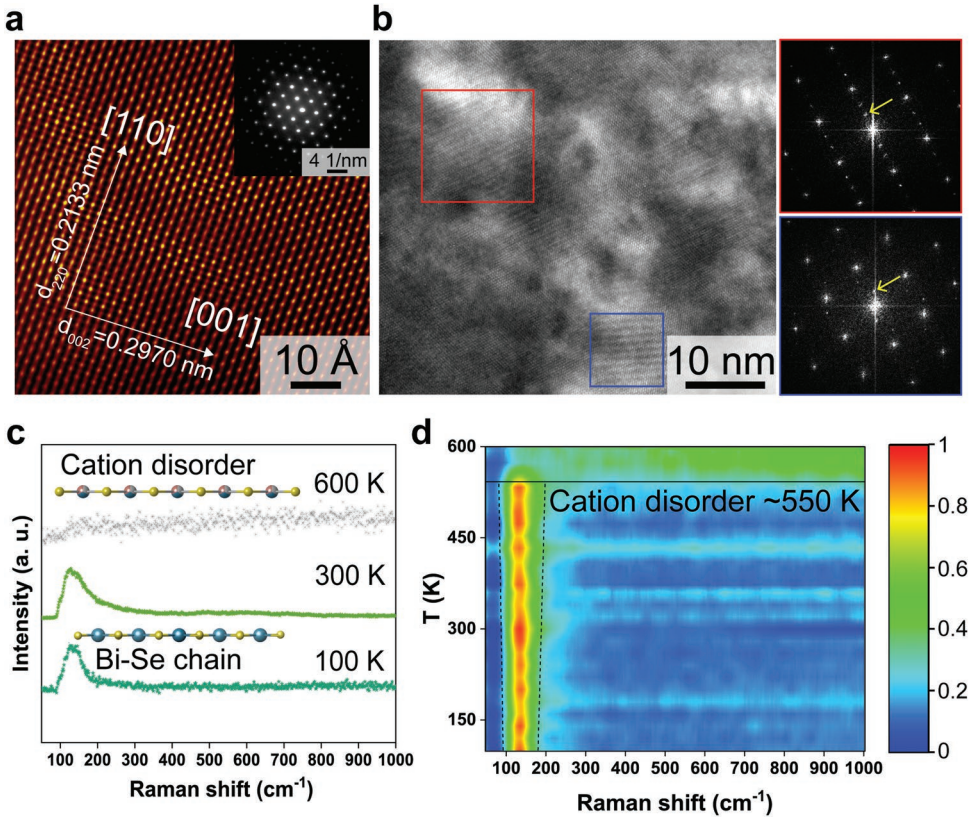

Figure 3. Temperature-dependent ordering and disordering of cations in ABSS05. a) Atom-resolved HAADF–STEM image of the matrix along the [110] zone axis. Periodic contrast ripples show a local chemical fluctuation of cations at room temperature. Inset is the SAED pattern of the analyzed region. b) HRTEM image and corresponding FFT images of the boxed regions, showing an existence of cation ordering. c) Selected Raman spectra at 100, 300, and 600 K. The peak from Bi–Se chain disappears due to cation disordering at high temperatures. d) 2D temperature-dependent Raman intensity plot of ABSS05. An estimated onset temperature for cation disordering is ≈550 K.

profile (2.5 nm). Moreover, contrast variation exists along [110] in both ABSS05 and $AgSbTe_2$.[18] Dark-field and high-resolution TEM images also confirm the existence of superstructures, implying an inherent inhomogeneity in cubic-stabilized $AgBiSe_2$ (Figure S4, Supporting Information).

However, the observed cation ordering disappears at ≈550 K according to our in situ Raman spectroscopy results (Figure 3c,d). It is known that hexagonal $AgBiSe_2$ exhibits two Raman-active modes for Bi—Se bonds: E_g and A_{1g} at 124 and 157 cm^{-1}, respectively.[11,22] However, we could only observe a peak at 130 cm^{-1} at both 100 and 300 K because E_g and A_{1g} vibrations become indistinguishable due to the isotropic nature of the cubic phase, which is in agreement with a previous study.[11] This characteristic peak disappears at 550 K, meaning that the long-range order of Bi—Se bonding is disrupted. When such antisite disorder dominates at high temperatures, the macroscopic polarizability from regular Bi—Se bonds disappears. Therefore, Raman spectroscopy confirms that cation disordering is promoted at high temperatures.

2.3. Defect Calculations Explain the n-Type Conductivity of $AgBiSe_2$-Based Alloys

We explain the poor p-type dopability of $AgBiSe_2$-based materials by calculating the point defect energetics of the end member $AgBiSe_2$ in the $L1_1$ phase using density functional theory (DFT) calculations. In principle, one can examine the formation of point defects in the disordered ABSS alloy using, for example, special quasi-random structures (SQS);[23] however, we show that our results of $AgBiSe_2$ match experimental observations well and provide first-order insights into the unstable p-type conductivity in $AgBiSe_2$-based materials.

The $L1_1$ structure of $AgBiSe_2$ can be constructed by expanding Ag–Se–Bi–Se–Ag–Se–Bi–Se... chains in all periodic directions (**Figure 4**a).[8] In other words, Ag, Bi, and Se planes are periodically stacked normal to the [111] direction. In the relaxed structure, we could find a rhombohedral distortion where the cuboid edge angle is 88° instead of 90°. This distortion is consistent with the weak DSC peak in ABSS07 and $AgBiSe_2$–PbSe alloys,[16] which may arise from an increase in the bonding angle to 90°. The crystallographic information of the relaxed $L1_1$ $AgBiSe_2$ can be found in Supporting Information (Table S1, Supporting Information).

Xiao et al. reported that solution-processed undoped $AgBiSe_2$ nanoparticles show a p–n–p transition in the conductivity type upon heating to 700 K.[11] Their calculation results showed that the Ag vacancy (V_{Ag}) has a low formation energy in the hexagonal phase, thereby suggesting that the defect is responsible for p-type conductivity in both the $L1_1$ and $D4$ structures. Unfortunately, these p-type properties have not been reproducible, and Pan et al. attributed the difference to impurity

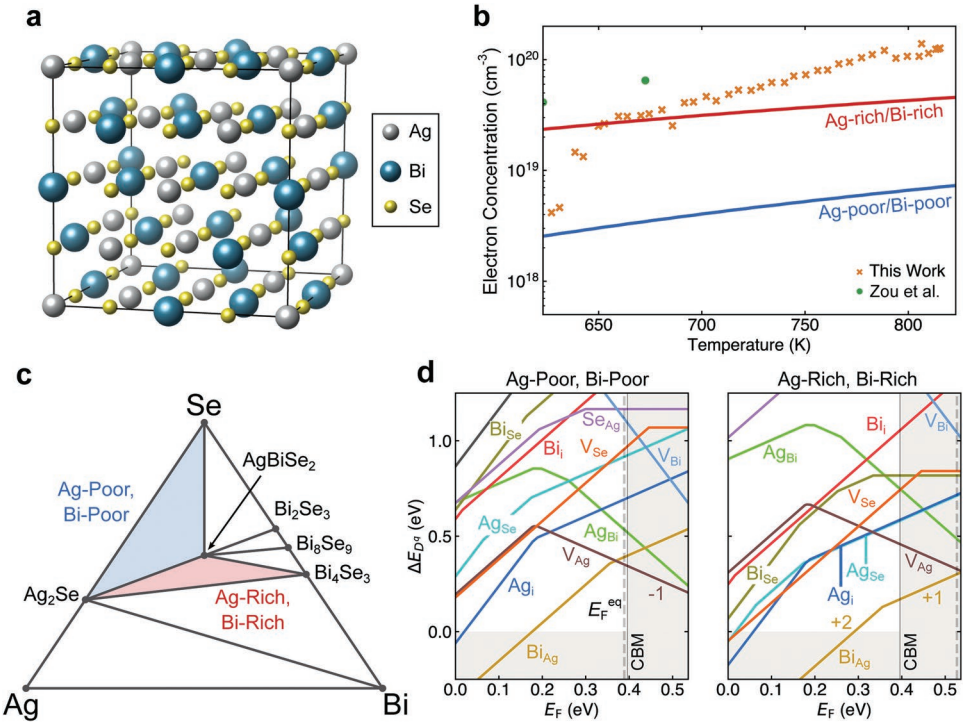

Figure 4. Native point defects in ordered cubic $AgBiSe_2$. a) Crystal structure of cubic $AgBiSe_2$ with $L1_1$ cation ordering. b) Calculated temperature-dependent carrier concentration of $AgBiSe_2$ for the $L1_1$ structure. c) Ternary Ag–Bi–Se phase diagram and equilibrium phases utilized for defect formation energy calculation. d) Calculated formation energy of possible point defects for Ag-poor/Bi-poor and Ag-rich/Bi-rich conditions.

contamination from the solution synthesis process.[10] Moreover, it is known that the formation energies of charged defects are sensitive to both the atomic chemical potentials and the Fermi level, neither of which are considered in the calculations conducted by Xiao et al.[24,25] Elemental chemical potentials depend not only on the intrinsic energies of each atom in the system, but they also depend on the thermodynamic conditions which are set by phase stability.[24,26] Therefore, we calculated the formation energies of point defects under different thermodynamic conditions of the Ag–Bi–Se ternary system (Figure 4c). Here, we show the formation energies of defects in $AgBiSe_2$ synthesized under two representative thermodynamic conditions: the Ag-poor/Bi-poor condition (when $AgBiSe_2$ is in equilibrium with Ag_2Se and elemental Se) and the Ag-rich/Bi-rich condition (when $AgBiSe_2$ is in equilibrium with Ag_2Se and Bi_4Se_3). Defect formation energies for other equilibrium phases can be found in the Supporting Information (Figure S5, Supporting Information).

Our calculations show that the low formation energy of the donor-like Bi-on-Ag antisite defect (Bi_{Ag}) is primarily responsible for the n-type conductivity of $AgBiSe_2$. In fact, $AgBiSe_2$ is natively n-type under all thermodynamic conditions, despite the considerably smaller density-of-states effective mass of electrons ($\approx 0.07m_0$) compared to that of holes ($\approx 0.87m_0$) (Figure S6, Supporting Information). This is evidenced by the equilibrium Fermi level, which is calculated from the defect formation energies and charge carrier concentrations by satisfying charge neutrality (see the Experimental Section). When $AgBiSe_2$ is synthesized under the most Ag-poor/Bi-poor condition, the Fermi level is 7 meV away from the conduction band edge (Figure 4d) and yields the lowest electron concentration (Figure 4b) due to charge compensation by holes generated by acceptor-like Ag vacancies (V_{Ag}). Indeed, the formation of V_{Ag} has been confirmed by positron annihilation spectroscopy in AgBiSeS[27] and $AgBiS_2$,[28] although p-type conductivity was not observed. On the other hand, the electron concentration is maximized when $AgBiSe_2$ is grown under Ag-rich/Bi-rich conditions (Figure 4b), when the Fermi level is 131 meV inside the conduction band (Figure 4d). The calculated electron concentration is within an order of magnitude of the experimental data for undoped $AgBiSe_2$ measured by Zou et al.[29] and this work (Figure 4b). Although discrepancies between the calculated and measured carrier concentrations can arise from, for example, self-doping effects in the $D4$ structure, the reasonable agreement with experiments indicates that the Bi_{Ag} antisite defect is responsible for the n-type conductivity in cubic $AgBiSe_2$.

It is known that the formation of antisite defects is stimulated when the electronegativity difference between atoms is small.[30] The thermochemical electronegativities of Ag, Bi, and Se are 2.88 and 2.69, 3.37, respectively.[31] Therefore, exchanging Ag and Bi would not significantly change the bonding characteristics. However, the formation energy of Ag_{Bi} is higher than that of Bi_{Ag} (Figure 4d), presumably due to the larger ionic radius of Ag^+ (115 pm) than that of Bi^{3+} (103 pm) in an octahedral site.[32] The lower formation energy of Bi_{Ag} is also supported by the integrated crystal orbital Hamilton population (ICOHP) (Table S2, Supporting Information), which provides an estimate of the bond covalency where more negative values correspond to stronger bonding interactions.[33] We find that Bi—Se bonding (ICOHP = –1.17 eV) is stronger than Ag—Se

bonding (ICOHP = –0.25 eV), explaining the facile formation of Bi_{Ag} defects.

The low formation energy of Bi_{Ag} in $AgBiSe_2$ is not entirely surprising, as cation disordering is prevalent in ABX_2 compounds and the defect was experimentally observed in hexagonal $AgBiSe_2$ by an XRD refinement study.[34] The finding however dispels the notion that Se vacancies are responsible for n-type conductivity, as was believed to be the dominant defect in hexagonal n-type $AgBiSe_2$.[35] Furthermore, the low formation energy of Bi_{Ag} was not expected from the DFT calculations by Xiao et al.,[11] and our calculations therefore demonstrate the importance of considering the dependence of defect formation energy on the Fermi level and phase equilibria.

The low formation energy of donor-like Bi_{Ag} obstructs efforts to dope $AgBiSe_2$ p-type. In general, a material is p-type dopable if all native donor defects have high formation energies; otherwise, holes generated by acceptor dopants will be compensated by electrons created by native donor defects. In other words, a sufficiently soluble acceptor dopant is necessary to stabilize p-type conductivity in $AgBiSe_2$ and to bypass charge carrier compensation by donor-like Bi_{Ag}. The unstable p-type character of cubic $AgBiSe_2$ when doped with Na (Figure 1c) can therefore be explained by the prevalence of donor-like Bi_{Ag} and low solubility of Na in the system, where holes generated by Na dopants are largely compensated by electrons generated by Bi_{Ag} defects. Accordingly, the calculations not only show that $AgBiSe_2$ is natively n-type due to the facile formation of donor-like Bi_{Ag}, but also that the cation antisite defect is the underlying obstacle forestalling p-type conductivity in the material.

While the defect thermodynamics discussed above show that $AgBiSe_2$ is natively n-type, explaining the difficulty in achieving p-type ABSS alloys may be more nuanced due to the presence of Sn in the system. Informed by the defect thermodynamics in $AgBiSe_2$, we propose that the repeated n-type conductivity in $AgBiSe_2$ (Figure 1b) can be explained by the formation of donor-like Bi_{Ag} under certain thermodynamic conditions. The formation energy of the cation antisite defect depends principally on two physical aspects: the bond strength with neighboring atoms and the chemical potentials of Bi and Ag. Since alloying $AgBiSe_2$ with SnSe does not change the anion sublattice, most cation sites will remain octahedrally-coordinated to Se in ABSS alloys as they are in unalloyed $AgBiSe_2$. Accordingly, the bonding strength between the Bi_{Ag} defect and the surrounding atoms in an ABSS alloy would be, to a first-order approximation, the same as in the end member $AgBiSe_2$. The chemical potentials on the other hand are established by phase equilibria with competing phases in the quaternary Ag–Bi–Sn–Se chemical space (Figure S7, Supporting Information). For example, both $AgBiSe_2$ and the ABSS alloy can be in equilibrium with Bi_8Se_9 and Bi_2Se_3 under certain thermodynamic conditions; under such conditions, the chemical potentials of Bi and Se are the same regardless of the compound, and only the chemical potential of Ag would be different. In fact, since the ABSS alloy is relatively Ag-poor compared to the end member $AgBiSe_2$, the formation energy of the donor-like Bi_{Ag} should be comparatively lower in the ABSS alloy compared to $AgBiSe_2$ when in equilibrium with Bi_8Se_9 and Bi_2Se_3. Accordingly, we hypothesize that the n-type conductivity and, more importantly, the poor p-type dopability, of ABSS alloys originates from donor-like Bi_{Ag} defects.

2.4. Probing Phase-Boundary Effects via Se Vapor Annealing

It can be reasoned that acceptor-like Sn vacancies (V_{Sn}) in ABSS alloys would induce p-type conductivity in the system; crystallographic characterization suggests that most Sn atoms are octahedrally-coordinated to Se (as if it were rock-salt SnSe), and orthorhombic SnSe (which is crystallographically equivalent to a strained rock-salt structure) is known to be intrinsically p-type due to V_{Sn}.[36] Indeed, the measured Seebeck coefficient of ABSS04 was 120 ± 1.2 μV K^{-1} at 323 K (**Figure 5**b). The positive sign of the Seebeck coefficient confirms that holes are the majority carrier in ABSS04. However, we found a large hysteresis of the Seebeck coefficient upon heating to 773 K under dynamic vacuum, and electrons became the majority carrier after cooling to 323 K. ABSS03 irreversibly lost its p-type conductivity at 773 K as well, signifying that this polarity reversal is common even in cubic-stabilized ABSS alloys (Figure S8a, Supporting Information). However, the Seebeck coefficient measured under He protection gas does not show any hysteresis and maintains p-type conductivity after a heating–cooling cycle, which might result from suppressed Se evaporation (Figures S8b and S9, Supporting Information). This observation can be explained by the DFT results, where Se-poor conditions (i.e., Ag-rich/Bi-rich conditions) result in the formation of donor-like Bi_{Ag} as depicted in Figure 5a. Because of the high volatility of Se at high temperatures, the dynamic vacuum environment promotes the loss of Se from the matrix, leading the system toward Se-poor thermodynamic conditions. However,

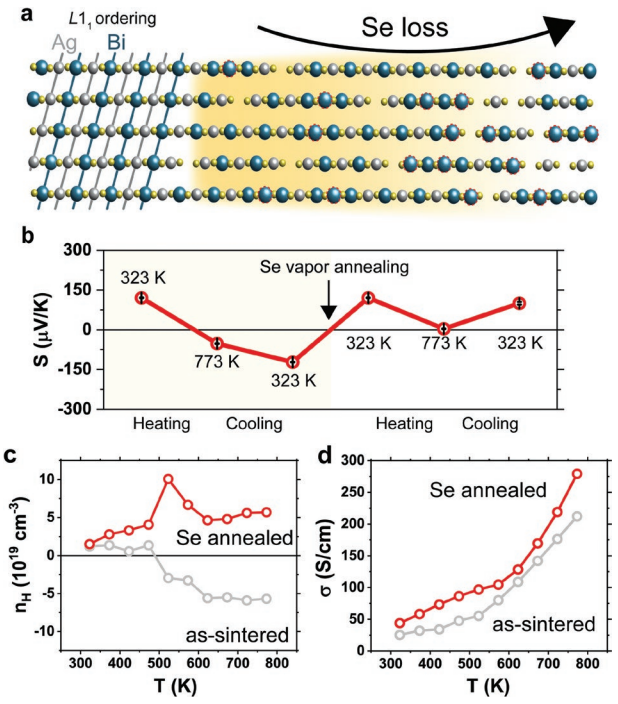

Figure 5. Se vapor annealing stabilizes the conductivity type. a) Schematic diagram of the effect of Se loss for Bi_{Ag} antisite defect formation. b) Change of Seebeck coefficient in ABSS04 upon heating–cooling cycles before and after Se vapor annealing. c,d) Temperature-dependent Hall carrier concentration (c) and the electrical conductivity in ABSS04 with Se vapor annealing (d).

He cover gas reduces the Se loss rate, resulting in an apparently stable Seebeck coefficient for several heating-cooling cycles.

Inspired by this, we use the saturation annealing technique to promote a Se-rich environment and, accordingly, prevent the formation of donor-like defects. Slight changes to the thermodynamic conditions of the sample, such as synthesizing the sample under Se-rich conditions as opposed to Se-poor conditions, may result in drastic alterations to the thermoelectric properties, a phenomenon arising from the phase boundary effects. Typically, saturation annealing is utilized to examine phase boundary effects by placing a sample in a saturating media having slight off-stoichiometric composition.[37] Given the complex chemical composition of this system, however, it might be challenging to accurately control the composition of the saturating media. Therefore, elemental Se was chosen as a saturating media for simplicity. By adding elemental Se to the sample and annealing it at 773 K in a sealed quartz tube for a sufficient amount of time, the sample is in equilibrium with Se vapor and therefore in a Se-rich condition. By crossing the phase boundary between a Se-poor and Se-rich condition, the formation energetics of intrinsic defects will become different, making some defects more or less favorable. A similar strategy was used to achieve n-type Mg_3Sb_2, where Mg vapor annealing was used to prevent the formation of acceptor-like Mg vacancies.[38]

As expected, p-type conductivity was recovered in ABSS04 after Se vapor annealing, leading to a Seebeck coefficient of $120 \pm 1\ \mu V\ K^{-1}$ and $4 \pm 1\ \mu V\ K^{-1}$ at 323 and 773 K, respectively. Note that this sample showed n-type conductivity at high temperatures before Se vapor annealing. This observation demonstrates the effects of phase boundary mapping to circumvent the low p-type dopability in $AgBiSe_2$-based thermoelectric alloys. High-temperature Hall measurements were conducted to gain insight into the polarity reversal (Figure 5c). The Hall carrier concentration of the as-sintered and annealed sample was $\approx 1 \times 10^{19}\ cm^{-3}$ at 323 K, which is consistent with the value of the Seebeck coefficient measured at 323 K. However, the as-sintered sample abruptly changed into an n-type semiconductor at 523 K, while the Se vapor-annealed sample maintained a high hole concentration up to 773 K. In addition, the electrical conductivity of the annealed sample was improved compared to that of the as-sintered sample, which may originate from grain growth during saturation annealing leading to the reduced grain boundary scattering and improved carrier mobility (Figure 5d). TE properties of other ABSS alloys after Se vapor annealing are shown in Figure S10, Supporting Information.

2.5. Change of Electronic Properties in p-Type ABSS Alloys

While electronic properties of Sb-based p-type cubic chalcogenide materials (e.g., $AgSbSe_2$[39] and $AgSbTe_2$[40]) have been extensively studied before, those of p-type cubic $AgBiSe_2$ have been unknown to date because of the aforementioned phase boundary effect. However, SnSe alloying coupled with Se vapor annealing enables future sophisticated investigations of the electronic properties of p-type cubic $AgBiSe_2$. Especially, heavy Bi atoms would have considerable spin-orbit coupling (SOC) effect,[8] while cubic SnSe is expected to show topological features in its band structure.[14] Therefore, we speculate that the electronic properties of ABSS alloys would be unique from those of conventional TE materials.

ABSS alloys showed an increasing electrical conductivity with increasing temperature despite their high carrier concentration (**Figure 6**a; Figure S10b and Table S3, Supporting Information). Moreover, ABSS05 showed a simultaneous increase of the Seebeck coefficient and the electrical conductivity with increasing temperature. Although this peculiar behavior has been observed in some ABX_2-based compounds,[13,14,41] an underlying mechanism has not been discovered yet. However, we speculate that this unconventional temperature dependence of electrical properties might result from the cation disordering at high temperatures. Our DFT calculations on the electronic band structure of disordered $AgBiSe_2$ using SQS cell do not show a band gap (Figure S11, Supporting Information). Therefore, a disordering of cations will make the matrix exhibit metallic behavior with increasing temperature, and the system might show complicated electrical properties because of this.

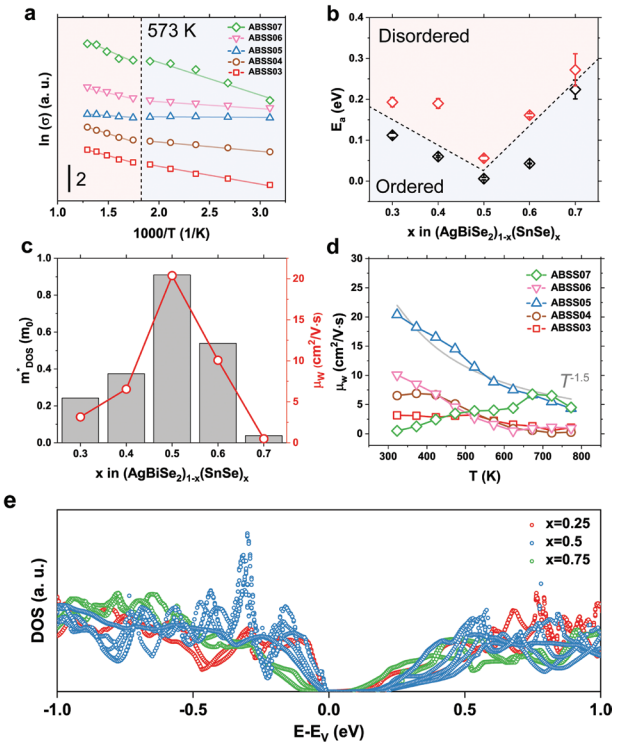

Figure 6. Effect of the cation on the electronic properties in ABSS alloys. a) Arrhenius plot of temperature-dependent electrical conductivities. The activation energy changes at 573 K. The lines were stacked for better visibility. b) The effect of cation disordering on the activation energy. The activation energies were obtained from the slope in (a). c) The change of density-of-states effective mass of holes (gray) and weighted mobility (red) at 323 K for various SnSe concentrations in ABSS alloys. d) Temperature-dependent weighted mobility of ABSS alloys. $T^{-1.5}$ dependence of deformation potential scattering (gray line) was drawn together for comparison. e) Calculated electronic density-of-states of $(AgBiSe_2)_{1-x}(SnSe)_x$ (x = 0.25, 0.5, 0.75) for 16 special quasi-random structure (SQS) cells.

Positive temperature dependence of the electrical conductivity implies a thermal activation of charge carriers mostly from a grain boundary resistance.[42] Moreover, a sudden increase of slope was observed after 573 K. The calculated activation energy from the slope is shown in Figure 6b. The activation energy decreased from $x = 0.3$ to $x = 0.5$, and increased afterward with SnSe alloying. ABSS05 showed the minimum value of 0.006 ± 0.003 eV, which is considerably lower than that of ABSS03 (0.112 ± 0.005 eV). However, the activation energy increased in all samples for temperatures above 573 K, signifying that the charge carrier scattering is intensified at high temperatures.

We now demonstrate how electronic properties change with SnSe alloying in cubic phase $AgBiSe_2$. Figure 6c shows the calculated density-of-states effective mass (m^*_{DOS}) and the weighted mobility (μ_w) of ABSS alloys at 323 K from the Seebeck coefficient and Hall effect measurements. It is known that μ_w is relatively insensitive to the change of the carrier concentration so that it enables an intuitive analysis of band movement and its effects on charge transport properties.[43] Unlike the activation energy, both m^*_{DOS} and μ_w are maximized in $x = 0.5$ ($AgBiSnSe_3$). The increase in m^*_{DOS} can result from an increased band effective mass (m^*_b) or the valley degeneracy (N_v) of the valence band. The former, however, is not beneficial for improving the TE properties because high band effective mass degrades the carrier mobility and electrical conductivity. On the other hand, increasing the valley degeneracy does not deteriorate the overall electrical mobility while increasing m^*_{DOS}, unless there is significant intervalley scattering.[44] It is known that μ_w and m^*_{DOS} are expressed by following Equations (1) and (2)

$$\mu_w = \mu_0 \left(\frac{m^*_{DOS}}{m_e} \right)^{3/2} \quad (1)$$

$$m^*_{DOS} = N_v^{2/3} m^*_b \quad (2)$$

where μ_0 is the mobility of a carrier at $k_B T$ higher than the band edge, and m_e is the free electron mass. For example, ABSS03 and 05 having m^*_{DOS} ratio of 3.76 should result in μ_w ratio of 7.3, which is close to the experimental value of 6.5. Therefore, improved μ_w does not mainly result from μ_0 but increased m^*_{DOS} in ABSS alloys. In addition, we can assume that m^*_b remains similar for all compositions given that the Hall mobilities do not change significantly (Table S3, Supporting Information). According to Equation (2), if we assume unchanged m^*_b, yielding 3.76-fold m^*_{DOS} requires the valley degeneracy ratio to be $(3.76)^{3/2} = 7.3$, which implies the convergence of another valence band with a larger N_v value in ABSS05. Temperature-dependent μ_w values are shown in Figure 6d. While most ABSS alloys show a thermal activation behavior at low temperatures, ABSS05 shows $T^{-1.5}$ dependence, which is a signature of deformation potential scattering. We speculate that the facile carrier transport of ABSS05 is related to the low activation energy observed in Figure 6b. The degree of cation ordering and corresponding energy barrier on charge carrier transport might be affected by SnSe concentration. We also estimated the changes in the band structure due to SnSe alloying using diffuse reflectance infrared Fourier transform spectroscopy (DRIFTS, Figure S12, Supporting Information). The band movement of $AgBiSe_2$ due to SnSe alloying is in accordance with the estimated m^*_{DOS}. In addition, DFT-calculated density-of-states of ABSS alloys for 16 SQS structures (Figure 6e), show a steep increase at the Fermi level near the valence band maximum at $x = 0.5$, which is consistent with the observed high m^*_{DOS} of ABSS05. Note that the change of the density-of-states near the Fermi level is important for determining transport properties since the derivative of the Fermi–Dirac statistics is included in the transport equation.[45] Calculated electronic band structures of ABSS alloys suggest that there might be complex effects such as band convergence or the emergence of new bands that contribute to the increased density-of-states (Figure S13, Supporting Information).

3. Conclusions

We have demonstrated that controlling cation disordering is crucial for achieving stable p-type cubic $AgBiSe_2$-based materials by Se vapor annealing. Transmission electron microscopy revealed the existence of cation ordering at room temperature, but in situ Raman spectroscopy also showed that cation disordering is promoted at high temperatures. With a combined understanding from experiments and computational results, we conclude that the Bi_{Ag} antisite defect is a predominant hole-killer, which can be regulated by the Se vapor annealing process to achieve stable p-type conductivity in ABSS alloys. Moreover, systematic transport property measurements revealed that the weighted mobility values of $AgBiSnSe_3$ are superior to those of other ABSS alloys owing to the increased density-of-states effective mass, which substantiate promising TE properties with further optimizations (e.g., carrier concentration). The findings of our work would be significant not only for understanding the behavior of multinary cubic thermoelectrics but also for controlling intrinsic defects in typical chalcogenide-based TE materials.

4. Experimental Section

Materials: Ag shots (99.99%, Alfa Aesar), Bi shots (99.999%, 5N Plus), Sn shots (99.999%, American Elements), and Se shots (99.999%, Alfa Aesar) were used without further purification.

Synthesis: The conventional melting and solidification method was used to synthesize polycrystalline $AgBiSe_2$–SnSe (ABSS) alloys. Stoichiometric amounts of elements were weighed and put into a carbon-coated quartz tube, and the tube was flame-sealed under a high-vacuum (≤10^{-4} Torr). Then, the elements were melted using a vertical tube furnace at 1273 K for 6 h, annealed at 773 K for 24 h, and cooled to room temperature using water quenching.

Densification: Synthesized ingots were pulverized into powder using agate mortar and pestle. Then, the powder was consolidated using an induction hot-pressing technique. A detailed description of the apparatus can be found elsewhere.[46] The powder was pressed using a uniaxial pressure of 50 MPa at 773 K for 10 min under an argon atmosphere. It should be noted that materials consolidated by spark plasma sintering (SPS) usually suffer from chemical inhomogeneity due to possible ion migration, especially for mobile cations.[47] Therefore, the chemical environment and corresponding defect energetics of hot-pressed and SPS-processed samples were considerably different.

Property Measurements: The temperature-dependent electrical conductivity and Hall coefficient were simultaneously measured

using a home-built Hall effect measurement system under a dynamic vacuum. The sample was electrically connected to the system using pressure-assisted Mo contacts with the van der Pauw configuration. Hall coefficients were measured using an excitation current of 100 mA under a 2 T magnetic field generated from a water-cooled electromagnet. The Seebeck coefficient of the sample was measured using chromel-Nb thermocouples by oscillating temperature gradient within 10 K under dynamic vacuum.[48] For the control experiment, the Seebeck coefficient of ABSS03 was measured under a weak He backpressure using a commercial apparatus (ZEM-3, ULVAC RIKO). The thermal conductivity was calculated using the following formula: $\kappa = \rho \times C_p \times D$, where ρ is the bulk density, C_p is the specific heat capacity, and D is the thermal diffusivity. The value of ρ was measured by the immersion method in isopropyl alcohol, while C_p was calculated using the Dulong–Petit law. D was measured using a laser flash apparatus (LFA 457, Netzsch) in an Ar atmosphere. A thin graphite coating was applied to the sample to increase the sample emissivity. Pulse-corrected Cowan model was used to calculate D values.

Selenium Vapor Annealing: Samples showing n-type transport properties were annealed at high temperatures with saturated Se vapor. Typically, 50 mg of Se shots were put into a quartz tube having 12.7 mm diameter and 10 cm length. Then, the sample was placed in a quartz tube while separated with elemental Se using quartz wool. The tube was flame-sealed under high vacuum, annealed at 773 K for at least 24 h, and cooled to room temperature using water quenching. Sample density did not change before and after Se vapor annealing, implying that the sample remains highly dense. Note that the sample was ground and polished to confirm that the property change is not originating from the surface effect.

Powder X-ray Diffraction: Powder XRD data were collected at room temperature on an X-ray diffractometer (SmartLab, Rigaku) equipped with a symmetric Johansson Ge(111) curved crystal monochromator (Cu$K_{\alpha 1}$ radiation, λ = 1.54056 Å) and 1D silicon strip detector (D/teX Ultra 250). The Cu X-ray tube was operated at 45 kV and 200 mA. The powder was sieved under 45 µm and packed on a glass holder. The intensity data from 20° to 80° were collected using a scan speed of 1° min^{-1}. The reproducibility of XRD measurements was confirmed by measuring identical samples at Northwestern University using an X-ray diffractometer (STADI P, STOE) with a transmission geometry (Figure S14, Supporting Information).

Differential Scanning Calorimetry: The heat flow measurement was experimentally obtained using a high-temperature differential scanning calorimeter (DSC Q2000, TA instrument). Samples were sealed using aluminum Tzero hermetic pan and lid (TA instrument, USA) and heated to 773 K with a ramping rate of 5 K min^{-1}.

In Situ Raman Spectroscopy: Temperature-dependent Raman spectra were acquired using a dispersive Raman spectrometer (ARAMIS, HORIBA Jobin Yvon). A 514 nm Ar-ion laser was used with a power of 0.3 mW and a diameter of 1 µm as an excitation source under a ×50 magnification. The sample was placed in a temperature control stage using a liquid nitrogen coolant and an electrical heater. The sample was sealed inside a stage using a stainless-steel cover with a quartz window for the measurement. Raman spectra ranging from 50 to 1000 cm^{-1} were measured for 1 s and accumulated five times using gratings with 1800 grooves. The spectra were obtained for at least three different positions using an encoder-controlled x-/y-motion stage. The signals were not processed except for averaging multiple spectra from various positions. Note that excessive laser power might cause a significant deformation on a sample surface. Therefore, an appropriate laser filter must be used for a reliable measurement.

Transmission Electron Microscopy: The specimen for TEM analysis was prepared by a focused ion beam (Helios G5 DualBeam, FEI) with liquid gallium metal as an ion source. The specimen was cut and milled to the final thickness of ≈20 nm to ensure electron transparency. The scanning TEM imaging was conducted by spherical aberration-corrected TEM (Titan Cubed G2 60–300, FEI) at 300 kV with a spherical aberration corrector (CEOS GmbH). To minimize electron drift, the measurement was started 24 h after sample loading. The size of the electron probe was ≈1 Å and the convergence semi-angle was 25.1 mrad. Energy-dispersive X-ray spectroscopy (EDX) elemental mapping was performed with four integrated silicon-drift EDX detectors (Super X, ChemiSTEM technology). The selected area electron diffraction (SAED) pattern was acquired with an aperture size of 100 nm. The acquired raw images were band-pass filtered to minimize background noise by using commercial software (HREM-Filters Lite, HREM Research Inc.).

Diffuse Reflectance Infrared Fourier Transform Spectroscopy: The optical reflectance of ABSS alloys was measured by Fourier transform infrared spectrometer (Nicolet iS50, Thermo Fisher) equipped with Smart Diffuse Reflectance accessories. Samples were diluted with KBr powders because of extremely high absorbance. The signals were recorded from 650 to 4000 cm^{-1} by mercury–cadmium–tellurium detectors which were cooled by liquid nitrogen. The reflectance spectra were accumulated 64 times and were converted to Kubelka–Munk function by $F(R) = (1-R)^2/2R$, where R is the reflectance.

Density Functional Theory Calculations: All first-principles DFT calculations were performed using the Vienna Ab initio Simulation Package (VASP)[49] under the projector-augmented wave method[50] and the Perdew–Burke–Ernzerhof (PBE) functional.[51] The plane-wave energy cutoff was set to 400 eV for all calculations, and a rotationally-invariant on-site Hubbard U correction was applied to Ag (U = 5 eV).[52] Due to the heavy Bi atom in the system, spin-orbit interactions were included in all total energy calculations, except for the structure optimization.[53] Defect formation energies were calculated using the standard supercell approach,[54,55] in which a 64-atom supercell of the $L1_1$ ordering of $AgBiSe_2$[8] was considered. The pylada-defects software[56] was used to automate point defect calculations. A 2 × 2 × 2 Γ-centered k-point mesh[57] was used to relax the ionic positions. The formation energy (ΔE_{D^q}) of a point defect D with charge state q was calculated as

$$\Delta E_{D^q} = E_{D^q} - E_{Host} - \sum_i n_i \mu_i + qE_F + E_{corr} \quad (3)$$

where E_{D^q} and E_{Host} are the total energies of the supercell with and without the defect respectively. The Fermi level E_F spans between the valence band and conduction band edges, and the band edge positions are therefore crucial for calculating the defect formation energies and charge carrier concentrations. To mitigate the well-known band gap underestimation of the GGA functional, a shift was applied to the band edge positions based on GW quasiparticle energy calculations, resulting in a valence band edge energy of E_{VBM} = 3.845 eV and a band gap of E_g = 0.396 eV. The chemical potential μ_i of element i is the energy of an atom that is either added ($n_i > 0$) or removed ($n_i < 0$) to create the defect. The chemical potential had two contributions, one from the reference state μ_i^0 and another from phase stability conditions $\Delta\mu_i$; together, the chemical potential could be expressed relative to the reference state as $\mu_i = \mu_i^0 + \Delta\mu_i$. The reference energies μ_i^0 were fitted to experimental formation enthalpies of known compounds in the Ag–Bi–Se ternary phase space, where the fitted values are tabulated in Table S5, Supporting Information. The bounds of the chemical potentials, $\Delta\mu_i$, on the other hand were determined such that $AgBiSe_2$ was stable and that competing phases were unstable. In Table S6, Supporting Information, the chemical potentials of each element in each of the five equilibrium phase regions in which $AgBiSe_2$ is stable was tabulated. Corrections to the defect formation energies were included,[55] which accounted for three fictitious effects arising from finite-size effects: i) potential misalignment between supercells with and without the defect; ii) long-range electrostatic interactions between periodic image charges; and iii) Moss–Burstein[58] band filling effects for shallow defects. The carrier concentration was calculated by satisfying the charge neutrality condition

$$\sum_{D^q} \left[qN_D e^{-\frac{\Delta E_{D^q}}{k_B T}} \right] + p - n = 0 \quad (4)$$

where N_D is the site concentration, k_B is the Boltzmann constant, T is the temperature, and p and n are the free hole and electron concentrations, respectively. The free carrier concentrations are calculated according to

$$p = \int_{-\infty}^{E_{VBM}} g(E)(1 - f(E))\mathrm{d}E \quad (5)$$

$$n = \int_{E_{CBM}}^{\infty} g(E) f(E)\mathrm{d}E \quad (6)$$

where $g(E)$ is the density of states and $f(E)$ is the Fermi–Dirac distribution. The density of states was calculated using the tetrahedron method and a k-point grid of $8 \times 8 \times 8$ and is shown in Figure S13, Supporting Information.

Models of $AgBiSe_2$-based alloys were constructed using SQS,[59] which were generated using the Alloy Theoretic Automated Toolkit.[60] Supercells containing 32 atoms were generated using a cutoff of 13.6 Å for both pairs and triplet clusters. The effective band structures of the alloy systems were calculated using the BandUP code,[61] which used an unfolding technique[62] in which the bands in the SQS supercell were mapped to the primitive cell Brillouin zone. To distinguish the effects of alloying SnSe on the electronic structure of $AgBiSe_2$ from the effects of intrinsic cation disordering between Ag and Bi atoms, initially the electronic structure of cation-disordered (SQS) $AgBiSe_2$ was calculated without Sn in the system. This model of unalloyed $AgBiSe_2$ showed no band gap (see Figure S11, Supporting Information), suggesting that the $L1_1$ ordering of Ag and Bi atoms is necessary for a bandgap to exist. Then 16 SQS supercells were generated at three compositions of $(AgBiSe_2)_{1-x}(SnSe)_x$ alloys ($x = 0.25, 0.5, 0.75$) without disrupting the $L1_1$ ordering of Ag and Bi atoms, yielding 48 unique SQS supercells.

Sound Velocity Measurements: The speed of sound was measured by the pulse-echo method, where an initial stress wave of ultrasonic pulse was sent and received by an identical piezoelectric transducer.[63] A longitudinal transducer with a center frequency of 5 MHz (CMR-052, ndtXducer) and a normal incidence shear transducer with an identical frequency (SM-052, ndtXducer) for measuring longitudinal and transverse sound velocities were used, respectively. The ultrasonic pulse signals were manipulated using an ultrasonic pulser/receiver (DPR 300, JSR Ultrasonics) and corresponding waveform was recorded using a digital oscilloscope (DSO-X 2022A, Keysight). A typical waveform contained three time delays for each measurement, and three measurements were conducted, yielding nine individual sound velocity measurements. The time delay, t_d, between back wall echoes was determined by varying t_d to maximize the cross-correlation, which is given by $\sum_t A_n(t)A_{n+1}(t - t_d)$.[64] Then, the speed of sound is calculated by $v = 2\,h/t_d$, where h is the sample thickness.

Multislice Simulations: HAADF images were simulated by a Dr. Probe multislice image simulator, which consider an effect of thermal diffuse scattering using the frozen phonon method.[65] Disordered crystal structure was used to simulate HAADF images of ABSS05, where Ag, Bi, and Sn has an occupancy of 1/3 in a same cation site. Microscope parameters were set according to the experimental values, and aberrations were neglected.

Supporting Information

Supporting Information is available from the Wiley Online Library or from the author.

Acknowledgements

This work was supported by the Creative Materials Discovery Program through the National Research Foundation of the Republic of Korea (NRF) funded by the Ministry of Science and ICT (No. 2020M3D1A1110501). This work made use of the Keck-II facility of Northwestern University's NUANCE Center, which has received support from the SHyNE Resource (NSF ECCS-2025633), the IIN, and Northwestern's MRSEC program (NSF DMR-1720139). This work also made use of the IMSERC X-RAY facility at Northwestern University, which has received support from the Soft and Hybrid Nanotechnology Experimental (SHyNE) Resource (NSF ECCS-2025633), and Northwestern University. The authors acknowledge Dr. Jin-Seok Choi at the KAIST Analysis center for Research Advancement (KARA) for STEM imaging. M.Y.T. was funded by the United States Department of Energy through the Computational Science Graduate Fellowship (DOE CSGF) under grant number DE-SC0020347. Work by J.P.M. was supported by a National Aeronautics and Space Administration (NASA) Space Technology Graduate Research Opportunity. J.P.M. and G.J.S. thank the award 70NANB19H005 from the U.S. Department of Commerce, National Institute of Standards and Technology, as part of the Center for Hierarchical Materials Design (CHiMaD).

Conflict of Interest

The authors declare no conflict of interest.

Data Availability Statement

The data that support the findings of this study are available from the corresponding author upon reasonable request.

Keywords

cation disordering, defect engineering, point defects, saturation annealing, thermoelectrics

Received: May 7, 2022
Revised: July 2, 2022
Published online: August 21, 2022

[1] G. J. Snyder, E. S. Toberer, *Nat. Mater.* **2008**, *7*, 105.
[2] J. He, T. M. Tritt, *Science* **2017**, *357*, eaak9997.
[3] J. P. Heremans, V. Jovovic, E. S. Toberer, A. Saramat, K. Kurosaki, A. Charoenphakdee, S. Yamanaka, G. J. Snyder, *Science* **2008**, *321*, 554.
[4] W. G. Zeier, A. Zevalkink, Z. M. Gibbs, G. Hautier, M. G. Kanatzidis, G. J. Snyder, *Angew. Chem., Int. Ed.* **2016**, *55*, 6826.
[5] E. J. Skoug, D. T. Morelli, *Phys. Rev. Lett.* **2011**, *107*, 235901.
[6] M. D. Nielsen, V. Ozolins, J. P. Heremans, *Energy Environ. Sci.* **2013**, *6*, 570.
[7] D. T. Morelli, V. Jovovic, J. P. Heremans, *Phys. Rev. Lett.* **2008**, *101*, 035901.
[8] H. Jang, S. Abbey, W. H. Nam, B. Frimpong, C. V. Nguyen, S.-J. Joo, H. S. Shin, J. Y. Song, E. N. Cho, M. Kim, Y. S. Jung, M.-W. Oh, *J. Mater. Chem. A* **2021**, *9*, 4648.
[9] a) J. D. Sugar, D. L. Medlin, *J. Alloys Compd.* **2009**, *478*, 75; b) Y. Goto, A. Nishida, H. Nishiate, M. Murata, C. H. Lee, A. Miura, C. Moriyoshi, Y. Kuroiwa, Y. Mizuguchi, *Dalton Trans.*. **2018**, *47*, 2575.
[10] L. Pan, D. Bérardan, N. Dragoe, *J. Am. Chem. Soc.* **2013**, *135*, 4914.
[11] C. Xiao, X. Qin, J. Zhang, R. An, J. Xu, K. Li, B. Cao, J. Yang, B. Ye, Y. Xie, *J. Am. Chem. Soc.* **2012**, *134*, 18460.
[12] a) Y. Luo, T. Xu, Z. Ma, D. Zhang, Z. Guo, Q. Jiang, J. Yang, Q. Yan, M. G. Kanatzidis, *J. Am. Chem. Soc.* **2021**, *143*, 13990; b) G. Liang, T. Lyu, L. Hu, W. Qu, S. Zhi, J. Li, Y. Zhang, J. He, J. Li, F. Liu, C. Zhang, W. Ao, H. Xie, H. Wu, *ACS Appl. Mater. Interfaces* **2021**, *13*, 47081; c) A. Suwardi, J. Cao, L. Hu, F. Wei, J. Wu, Y. Zhao, S. H. Lim, L. Yang, X. Y. Tan, S. W. Chien, Y. Yin, W.-X. Zhou, W. L. Mun Nancy, X. Wang, S. H. Lim, X. Ni, D. Li, Q. Yan, Y. Zheng, G. Zhang, J. Xu, *J. Mater. Chem. A* **2020**, *8*, 18880.

[13] S. Roychowdhury, T. Ghosh, R. Arora, U. V. Waghmare, K. Biswas, *Angew. Chem., Int. Ed.* **2018**, *57*, 15167.
[14] S. Chandra, R. Arora, U. V. Waghmare, K. Biswas, *Chem. Sci.* **2021**, *12*, 13074.
[15] M. Dutta, K. Pal, U. V. Waghmare, K. Biswas, *Chem. Sci.* **2019**, *10*, 4905.
[16] H. Zhu, T. Zhao, B. Zhang, Z. An, S. Mao, G. Wang, X. Han, X. Lu, J. Zhang, X. Zhou, *Adv. Energy Mater.* **2021**, *11*, 2003304.
[17] S. N. Guin, V. Srihari, K. Biswas, *J. Mater. Chem. A* **2015**, *3*, 648.
[18] J. Ma, O. Delaire, A. F. May, C. E. Carlton, M. A. McGuire, L. H. VanBebber, D. L. Abernathy, G. Ehlers, T. Hong, A. Huq, W. Tian, V. M. Keppens, Y. Shao-Horn, B. C. Sales, *Nat. Nanotechnol.* **2013**, *8*, 445.
[19] a) K. Hoang, S. D. Mahanti, J. R. Salvador, M. G. Kanatzidis, *Phys. Rev. Lett.* **2007**, *99*, 156403; b) Y.-H. Ko, M.-W. Oh, J. K. Lee, S.-D. Park, K.-J. Kim, Y.-S. Choi, *Curr. Appl. Phys.* **2014**, *14*, 1538.
[20] E. Quarez, K.-F. Hsu, R. Pcionek, N. Frangis, E. K. Polychroniadis, M. G. Kanatzidis, *J. Am. Chem. Soc.* **2005**, *127*, 9177.
[21] X. Hua, V. I. Hegde, C. Wolverton, *Chem. Mater.* **2019**, *31*, 9445.
[22] J. Zhang, Z. Peng, A. Soni, Y. Zhao, Y. Xiong, B. Peng, J. Wang, M. S. Dresselhaus, Q. Xiong, *Nano Lett.* **2011**, *11*, 2407.
[23] J. Qu, A. Balvanz, S. Baranets, S. Bobev, P. Gorai, *Mater. Horiz.* **2022**, *9*, 720.
[24] M. Y. Toriyama, J. Qu, G. J. Snyder, P. Gorai, *J. Mater. Chem. A* **2021**, *9*, 20685.
[25] A. Goyal, P. Gorai, S. Anand, E. S. Toberer, G. J. Snyder, V. Stevanović, *Chem. Mater.* **2020**, *32*, 4467.
[26] a) S. Ohno, K. Imasato, S. Anand, H. Tamaki, S. D. Kang, P. Gorai, H. K. Sato, E. S. Toberer, T. Kanno, G. J. Snyder, *Joule* **2018**, *2*, 141; b) M. Wood, M. Y. Toriyama, S. Dugar, J. Male, S. Anand, V. Stevanović, G. J. Snyder, *Adv. Energy Mater.* **2021**, *11*, 2100181; c) L. Fu, K. H. Lee, S.-I. Kim, J.-H. Lim, W. Choi, Y. Cheng, M.-W. Oh, Y.-M. Kim, S. W. Kim, *Acta Mater.* **2021**, *215*, 117058.
[27] S. N. Guin, S. Banerjee, D. Sanyal, S. K. Pati, K. Biswas, *Chem. Mater.* **2017**, *29*, 3769.
[28] S. N. Guin, S. Banerjee, D. Sanyal, S. K. Pati, K. Biswas, *Inorg. Chem.* **2016**, *55*, 6323.
[29] M. Zou, Q. Liu, C.-F. Wu, T.-R. Wei, Q. Tan, J.-F. Li, F. Chen, *RSC Adv.* **2018**, *8*, 7055.
[30] a) M. W. Oh, J. H. Son, B. S. Kim, S. D. Park, B. K. Min, H. W. Lee, *J. Appl. Phys.* **2014**, *115*, 133706; b) P. Gorai, A. Ganose, A. Faghaninia, A. Jain, V. Stevanović, *Mater. Horiz.* **2020**, *7*, 1809; c) J. H. Son, M. W. Oh, B. S. Kim, S. D. Park, B. K. Min, M. H. Kim, H. W. Lee, *J. Alloys Compd.* **2013**, *566*, 168; d) J. B. Vaney, J. Carreaud, G. Delaizir, A. Piarristeguy, A. Pradel, E. Alleno, J. Monnier, E. B. Lopes, A. P. Gonçalves, A. Dauscher, C. Candolfi, B. Lenoir, *J. Mater. Chem. C* **2016**, *4*, 2329.
[31] C. Tantardini, A. R. Oganov, *Nat. Commun.* **2021**, *12*, 2087.
[32] R. Shannon, *Acta Crystallogr.* **1976**, *32*, 751.
[33] X. Zhang, D. Wang, G. Wang, L.-D. Zhao, *Ceram. Int.* **2019**, *45*, 14953.
[34] F. Böcher, S. P. Culver, J. Peilstöcker, K. S. Weldert, W. G. Zeier, *Dalton Trans.* **2017**, *46*, 3906.
[35] a) S. Li, Z. Feng, Z. Tang, F. Zhang, F. Cao, X. Liu, D. J. Singh, J. Mao, Z. Ren, Q. Zhang, *Chem. Mater.* **2020**, *32*, 3528; b) D. S. Parker, A. F. May, D. J. Singh, *Phys. Rev. Appl.* **2015**, *3*, 064003.
[36] a) Y. Zhou, W. Li, M. Wu, L.-D. Zhao, J. He, S.-H. Wei, L. Huang, *Phys. Rev. B* **2018**, *97*, 245202; b) Y. Huang, C. Wang, X. Chen, D. Zhou, J. Du, S. Wang, L. Ning, *RSC Adv.* **2017**, *7*, 27612.
[37] a) J. Male, M. T. Agne, A. Goyal, S. Anand, I. T. Witting, V. Stevanović, G. J. Snyder, *Mater. Horiz.* **2019**, *6*, 1444; b) P. Jood, J. P. Male, S. Anand, Y. Matsushita, Y. Takagiwa, M. G. Kanatzidis, G. J. Snyder, M. Ohta, *J. Am. Chem. Soc.* **2020**, *142*, 15464.
[38] M. Wood, J. J. Kuo, K. Imasato, G. J. Snyder, *Adv. Mater.* **2019**, *31*, 1902337.
[39] a) S. N. Guin, A. Chatterjee, D. S. Negi, R. Datta, K. Biswas, *Energy Environ. Sci.* **2013**, *6*, 2603; b) Z. Huang, S. A. Miller, B. Ge, M. Yan, S. Anand, T. Wu, P. Nan, Y. Zhu, W. Zhuang, G. J. Snyder, P. Jiang, X. Bao, *Angew. Chem., Int. Ed.* **2017**, *56*, 14113.
[40] a) S. Roychowdhury, T. Ghosh, R. Arora, M. Samanta, L. Xie, N. K. Singh, A. Soni, J. He, U. V. Waghmare, K. Biswas, *Science* **2021**, *371*, 722; b) J. K. Lee, B. Ryu, S. Park, J. H. Son, J. Park, J. Jang, M.-W. Oh, S. Park, *Acta Mater.* **2022**, *222*, 117443.
[41] a) Y. Luo, S. Hao, S. Cai, T. J. Slade, Z. Z. Luo, V. P. Dravid, C. Wolverton, Q. Yan, M. G. Kanatzidis, *J. Am. Chem. Soc.* **2020**, *142*, 15187; b) M. Dutta, M. V. D. Prasad, J. Pandey, A. Soni, U. V. Waghmare, K. Biswas, *Angew. Chem., Int. Ed.* **2022**, *61*, 202200071.
[42] J. J. Kuo, S. D. Kang, K. Imasato, H. Tamaki, S. Ohno, T. Kanno, G. J. Snyder, *Energy Environ. Sci.* **2018**, *11*, 429.
[43] G. J. Snyder, A. H. Snyder, M. Wood, R. Gurunathan, B. H. Snyder, C. Niu, *Adv. Mater.* **2020**, *32*, 2001537.
[44] J. Park, M. Dylla, Y. Xia, M. Wood, G. J. Snyder, A. Jain, *Nat. Commun.* **2021**, *12*, 3425.
[45] a) T. Thonhauser, T. J. Scheidemantel, J. O. Sofo, J. V. Badding, G. D. Mahan, *Phys. Rev. B* **2003**, *68*, 085201; b) M. W. Oh, D. M. Wee, S. D. Park, B. S. Kim, H. W. Lee, *Phys. Rev. B* **2008**, *77*, 165119.
[46] A. D. LaLonde, T. Ikeda, G. J. Snyder, *Rev. Sci. Instrum.* **2011**, *82*, 025104.
[47] a) J. L. Cui, W. J. Xiu, L. D. Mao, P. Z. Ying, L. Jiang, X. Qian, *J. Solid State Chem.* **2007**, *180*, 1158; b) M. Beekman, M. Baitinger, H. Borrmann, W. Schnelle, K. Meier, G. S. Nolas, Y. Grin, *J. Am. Chem. Soc.* **2009**, *131*, 9642.
[48] S. Iwanaga, E. S. Toberer, A. LaLonde, G. J. Snyder, *Rev. Sci. Instrum.* **2011**, *82*, 063905.
[49] a) G. Kresse, J. Furthmüller, *Comput. Mater. Sci.* **1996**, *6*, 15; b) G. Kresse, J. Furthmüller, *Phys. Rev. B* **1996**, *54*, 11169.
[50] P. E. Blöchl, *Phys. Rev. B* **1994**, *50*, 17953.
[51] J. P. Perdew, K. Burke, M. Ernzerhof, *Phys. Rev. Lett.* **1996**, *77*, 3865.
[52] a) S. L. Dudarev, G. A. Botton, S. Y. Savrasov, C. J. Humphreys, A. P. Sutton, *Phys. Rev. B* **1998**, *57*, 1505; b) V. Stevanović, S. Lany, X. Zhang, A. Zunger, *Phys. Rev. B* **2012**, *85*, 115104; c) P. Gorai, E. S. Toberer, V. Stevanović, *Phys. Chem. Chem. Phys.* **2016**, *18*, 31777.
[53] a) A. Goyal, P. Gorai, E. S. Toberer, V. Stevanović, *npj Comput. Mater.* **2017**, *3*, 42; b) D. West, Y. Y. Sun, H. Wang, J. Bang, S. B. Zhang, *Phys. Rev. B* **2012**, *86*, 121201; c) J. Pan, W. K. Metzger, S. Lany, *Phys. Rev. B* **2018**, *98*, 054108.
[54] a) C. Freysoldt, B. Grabowski, T. Hickel, J. Neugebauer, G. Kresse, A. Janotti, C. G. Van de Walle, *Rev. Mod. Phys.* **2014**, *86*, 253; b) S. Lany, A. Zunger, *Modell. Simul. Mater. Sci. Eng.* **2009**, *17*, 084002.
[55] S. Lany, A. Zunger, *Phys. Rev. B* **2008**, *78*, 235104.
[56] A. Goyal, P. Gorai, H. Peng, S. Lany, V. Stevanović, *Comput. Mater. Sci.* **2017**, *130*, 1.
[57] H. J. Monkhorst, J. D. Pack, *Phys. Rev. B* **1976**, *13*, 5188.
[58] E. Burstein, *Phys. Rev.* **1954**, *93*, 632.
[59] a) A. Zunger, S. Wei, L. G. Ferreira, J. E. Bernard, *Phys. Rev. Lett.* **1990**, *65*, 353; b) S. Wei, L. G. Ferreira, J. E. Bernard, A. Zunger, *Phys. Rev. B: Condens. Matter Mater. Phys.* **1990**, *42*, 9622.
[60] A. van de Walle, P. Tiwary, M. de Jong, D. L. Olmsted, M. Asta, A. Dick, D. Shin, Y. Wang, L. Q. Chen, Z. K. Liu, *Calphad* **2013**, *42*, 13.
[61] a) P. V. C. Medeiros, S. Stafstrom, J. Bjork, *Phys. Rev. B* **2014**, *89*, 041407; b) P. V. C. Medeiros, S. S. Tsirkin, S. Stafstrom, J. Bjork, *Phys. Rev. B* **2015**, *91*, 041116.
[62] V. Popescu, A. Zunger, *Phys. Rev. B* **2012**, *85*, 085201.
[63] H. Jang, S. Abbey, B. Frimpong, C. V. Nguyen, P. Ziolkowski, G. Oppitz, M. Kim, J. Y. Song, H. S. Shin, Y. S. Jung, M.-W. Oh, *ACS Appl. Mater. Interfaces* **2022**, *14*, 1270.
[64] R. Hanus, R. Gurunathan, L. Lindsay, M. T. Agne, J. Shi, S. Graham, G. Jeffrey Snyder, *Appl. Phys. Rev.* **2021**, *8*, 031311.
[65] J. Barthel, *Ultramicroscopy* **2018**, *193*, 1.